Segregation and Migration of Oxygen Vacancy in Σ3 (111) Tilt Grain Boundary of Ceria

Fenglin Yuan[a,*], Bin Liu[a], Yanwen Zhang[b,a] and William J. Weber[a,b,*]

[a] Department of Materials Science and Engineering, University of Tennessee, Knoxville, Tennessee 37996, USA

[b] Materials Science & Technology Division, Oak Ridge National Laboratory, Oak Ridge, Tennessee 37831, USA

Corresponding Author:

fyuan5@utk.edu; wjweber@utk.edu

Abstract

In nanocrystalline materials, defect-grain boundary (GB) interaction plays a key role in determining the structure stability, as well as size-dependent ionic, electronic, magnetic and chemical properties. In this study, we systematically investigated using density functional theory segregation and migration of oxygen vacancies at the $\Sigma 3\ [1\bar{1}0]/(111)$ grain boundary of ceria. Three oxygen layers near the GB are predicted to be segregation sites for oxygen vacancies. Moreover, the presence of oxygen vacancies stabilizes this tilt GB at a low Fermi level and/or oxygen poor conditions. An atomic strain model was proposed to rationalize layer dependency of the relaxation energy for +2 charged oxygen vacancy. The structural origin of large relaxation energies at layers 1 and 2 was determined to be free-volume space that induces ion relaxation towards the GB. Our results not only pave the way for improving the oxygen transport near GBs of ceria, but also provide important insights into engineering the GB structure for better ionic, magnetic and chemical properties of nanocrystalline ceria.

1. Introduction

Nano-crystalline ceramic (NCC) materials are known to possess interesting properties compared with their microcrystalline and bulk counterparts owing to the extreme large surface-to-volume ratio. The properties of NCC are often size-dependent, which gives an independent degree of freedom to tune a broad range of material properties, such as chemical[1–6], ionic[7,8], electrical[9], optical[10–13] and magnetic[14–17] properties. Two major factors contribute to such size-dependency: the first is the existence of planar defects, such as grain boundaries (GBs) and/or interfaces; the second is the interaction between planar defects and other characteristic structural defects including point defects and dislocations. Therefore, understanding of the interaction of defects with GBs and interfaces becomes crucial for optimizing NCC.

Cerium dioxide (i.e., Ceria or CeO_2) has attracted numerous research efforts due to application in radiation tolerant materials[18–20], chemical catalyst[1–6], oxygen sensors[21–23] and solid oxide fuel cell (SOFC)[24–26]. Nano-structured ceria (NSC) show desirable improvement over bulk ceria in various aspects, such as enhanced irradiation tolerance[18–20], increased catalytic efficiency at the metal-ceria interface[6] and efficiency for ceria reduction[27]. Formation and transport of oxygen vacancy (i.e., V_O), which are the fundamental processes central to applications of ceria, have been widely studied for the bulk case[28–30]. In practice, the unavoidable introduction of 2D defects such as surfaces or GBs complicate oxygen vacancy behavior owing to the interaction between vacancy and 2D defect. For example, oxygen vacancy can segregate nearby GB in Gd- and Mn-doped ceria[31], and oxygen vacancy can assume a subsurface ordering in reduced ceria (111) surfaces[32]. Nevertheless, knowledge is limited for oxygen vacancy behavior near grain

boundaries, which is critical for controlling the electron and ion behavior in an environment different from the bulk and the overall performance of NSC. Recent experiments[33,34] identified detailed structures of two GBs, $\Sigma 5\ [001]/(210)$ and $\Sigma 3\ [1\bar{1}0]/(111)$, in ceria and uncovered the importance of oxygen vacancy on the stability of the GBs. However, atomic scale characterization of non-stoichiometry and oxygen transport by experiments proved to be difficult due to the required use of advanced techniques, such as transmission electron microscope (TEM) with high voltage, chromatic and spherical aberration correction[33–36] and/or high resolution scanning tunneling microscope (STM)[37]. As an alternative to experiments, first-principle calculations achieved fruitful results in past decades, and proved to be a robust method for studying defect behavior in ceria[29,38–46].

The $\Sigma 3\ [1\bar{1}0]/(111)$ GB has a lower GB formation energy than the $\Sigma 5\ [001]/(210)$ GB because of less structural distortion and lower density of three-folded O (i.e., O bonded with three neighboring Ce ions) at the GB planes[34]. Since low formation energy indicates high population and contribution to NSC, we systematically investigated, utilizing first principle calculations, the oxygen vacancy formation and migration in the $\Sigma 3\ [1\bar{1}0]/(111)$ GB of ceria. Our results predict oxygen vacancy segregation in the nearest three atomic oxygen layers to the GB, and the presence of oxygen vacancies stabilizes this tilt GB at a low Fermi level and/or oxygen poor conditions. The $V_O^{\cdot\cdot}$ defect (i.e., V_O with +2 charge) dominates at low Fermi level and/or oxygen poor conditions, while the $V_O^{\times}$ defect (i.e., V_O with zero charge) appears at high Fermi level and in oxygen poor conditions. An atomic strain model was proposed to explain the layer dependence of

relaxation energies for $V_O^{\cdot\cdot}$. Free-volume space induced relaxation of first nearest neighbor Ce ions towards the GB was identified as the structural origin for large relaxation energies for $V_O^{\cdot\cdot}$ in two oxygen layers nearby GB. Based on our results, tailoring the ionic, magnetic and chemical properties of NSC may be achieved by controlling GB's structure and thickness as well as grain size.

2. Calculation Details

Density functional theory (DFT) simulations were performed using the projected augmented waves (PAW)[47,48] method in Vienna Ab initio Simulation Package (VASP)[49–52]. A local density approximation[53] coupled with the Hubbard on-site Columbic correction in Dudarev et al.'s formalism[54] (LDA+U) and spin polarized calculation were employed. We used a U=6 eV and J=0 eV to capture the localization into 4f orbitals of electrons[28,29]. A Monkhorst-Pack 4x2x1 k-mesh[55] and 400 eV[44,56] plane wave cutoff energy were used to ensure a converged and accurate result. The $\Sigma 3\ [1\bar{1}0]/(111)$ GB, which was generated by mirroring and shifting (111) plane, has 216 atoms and a dimension of 7.6 Å × 13.1 Å × 28.1 Å (Figure 1). Two GBs are included to resolve the conflict between periodic boundary condition (PBC) and stoichiometry, and the separation distance between two GBs within the cell is large enough to reduce GB-GB interaction. And the distance between two GBs across the cell is much larger than that within the cell, owing to the prevention of interference of GB on oxygen vacancies behavior under PBC. All structure visualizations were realized in VESTA[57], and atoms

were represented by solid spheres with ionic radii. Kröger–Vink notation[58] is used for all defects. Structural relaxations were performed through conjugate-gradient algorithm to minimize the Hellman-Feynman force below 0.01 eV/Å. All migration energy barriers for oxygen vacancies were calculated by the climbing-image nudged elastic band (CI-NEB) method[59]. Low GB formation energy (1 J/m^2) indicates relative high formation ability of ∑3 GBs, in agreement with recent experiments[34].

The defect formation energy was defined as:

$$E(form) = E(d) - E(p) + \sum_i n_i \mu_i + q(\Delta E_f + E_{vbm}) \quad (1)$$

where *E(d)* is the total energy after defect formation, *E(p)* the total energy before defect formation, n_i the total number of atoms removed during defect formation, μ_i the chemical potential for removed atoms, q the charge state of defect, E_{vbm} the valence band maximum, and ΔE_f the measured Fermi energy level from valence band maximum. The oxygen chemical potential range (-10.46 eV, -5.24 eV) was determined by two thermodynamic limits: (1) the limit of ceria stoichiometry: $\mu_{Ce} + 2\mu_O = \mu_{CeO_2}$; and (2) the limit of the system against the decomposition into constituent elements (face-centered-cubic single crystal of Ce and gaseous O_2): $\mu_{Ce} \le \mu_{Ce}^{Bulk}$ and $\mu_O \le \mu_O^{O_2}$. To quantify the formation ability of a vacancy at the GB in reference to bulk, segregation energy E_{seg} for V_O was calculated by:

$$E_{seg} = E_f(GB) - E_f(Bulk) \quad (2)$$

where $E_f(GB)$ and $E_f(Bulk)$ are the formation energy of V_O in GB and bulk, respectively. In addition, the formation energy of the non-stoichiometric GB, E_f^{NGB}, was determined by:

$$E_f^{NGB} = E(NGB) - E(pb) + \sum_i n_i \mu_i + q(\Delta E_f + E_{vbm}) \quad (3)$$

where *E(NGB)* is the energy for the supercell with the GB and one V_O, and *E(pb)* is the energy for corresponding bulk supercell without V_O.

3. Results and Discussions

3.1 Segregation of Oxygen Vacancies

The $\Sigma 3\ [1\bar{1}0]/(111)$ GB can be envisaged as alternating O and Ce planes (Figure 1), where two O planes meet with each other at the GBs. Oxygen planes are labeled according to their distance from the grain boundary (Figure 1). The larger the number is, the further oxygen layer is from the GB. Segregation energies as a function of oxygen layer were calculated for +2, +1 and 0 charged vacancies (i.e, $V_O^{\cdot\cdot}$, $V_O^{\cdot}$ and $V_O^{\times}$), as shown in Figure 2. It was observed that the near-GB layers (i.e., layers 0, 1 and 2) have negative segregation energies for vacancies, while the far-GB layers (i.e., layers 3, 4 and 5) have segregation energies near zero. The V_O segregation range bound by the GB and layer 2 was estimated to be about 0.5 nm from the GB. Our results predict that the ceria GB

favors accumulation of oxygen vacancies, but only strongly influences vacancy distribution in 0.5 nm from the GB.

Electronic transition levels are calculated based on equilibrium of defect formation energies between a pair of point defects, and, therefore, define the stability boundary for the corresponding defects. Figure 3 depicts the +1/0, +2/+1 transition levels of oxygen vacancies for GB and bulk. First, the transition levels from the GB gradually converged to that in bulk when the oxygen layer number exceeds 2 (i.e., at far-GB layers). Second, the $V_O^{\cdot}$ occupies a limited region compared with +2 and 0 charge cases in both GB and bulk, in agreement with a previous DFT study[60]. Third, it's worth noting that despite the fact that the boundaries of the +2/+1 transition at the GB and in the bulk unanimously lie below the lowest energy of 4f band, the remaining electrons at O vacancy site after the removal of oxygen atom localize into neighboring Ce 4f orbitals for both $V_O^{\cdot}$ and $V_O^{\times}$, which form polarons responsible for electron conduction[61] in ceria.

To fully explore oxygen vacancy forming ability, we plot the chemical potential and electronic Fermi level dependent oxygen vacancy formation energies in Figure 4 for two representative oxygen layers, 0 and 1. Stoichiometric region occupies about 50% of the whole explored region, and is dominant in an oxygen rich environment, in agreement with experimental results[34]. In oxygen poor conditions, +2, +1 and 0 charged oxygen vacancies form naturally, driven by the negative formation energies. The $V_O^{\cdot\cdot}$ occupies a low Fermi level and/or located in oxygen poor region, while the $V_O^{\times}$ on the other hand prefers a high Fermi level and oxygen poor region. The $V_O^{\cdot}$ is stable only in a limited region near GB layers, consistent with transition level calculations (Figure 2). In addition,

we explored how the oxygen vacancy influences GB's formation ability by mapping E_f^{NGB} with respect to Fermi level and chemical potential (Figure 5). The stoichiometric GBs are stable in an oxygen rich environment, and hence free from oxygen vacancy formation, while non-stoichiometric GBs appear at low Fermi levels and/or in oxygen poor conditions. The presence of one oxygen vacancy stabilizes the GB by reducing E_f^{NGB} from 0.87 eV in stoichiometric case to as low as 0.43 eV. It's crucial to be aware of the fact that our current study is limited to 0 K conditions. Temperature can drastically increase the oxygen vacancy concentration for the stoichiometric region defined in this study. The temperature- and pressure-effect on point defects in GB of ceria will be reported elsewhere.

The defect-induced structural relaxation can be decoupled into two consecutive relaxation processes: (1) electronic relaxation with fixed ion positions; and subsequent (2) ionic relaxation. Electronic relaxation energy or bond energy E_{bond} is measured by the energy difference between the supercell after fix-ion electronic relaxation and the pristine supercell. Ionic relaxation energy, E_{relax}, is calculated by subtracting the energy of the pristine supercell from that of the fully relaxed supercell. Provided E_b and E_r are defined by $E_b = E_{bond}^{GB} - E_{bond}^{Bulk}$ and $E_r = E_{relax}^{GB} - E_{relax}^{Bulk}$, respectively. We can, therefore, predict the segregation energies for V_O by $E_{seg} = E_b + E_r$. The aforementioned analysis[62] was carried out for GB and bulk, and the corresponding results are plotted in Figure 6(a). For near-GB layers, E_b increases and E_r decreases steadily with increasing oxygen layer number. For far-GB layers, both E_b and E_r decrease with increasing oxygen layer number. The large negative values of E_r at oxygen layers 0, 1 and 2 give rise to near-GB vacancy

segregation region identified in Figure 2. To better understand the layer dependency of E_r, an atomic strain model was proposed. In general, the removal of oxygen ion results in inward-vacancy relaxation of O neighbors and outward-vacancy relaxation of Ce neighbors. Since nearest neighbor ions constitute a major contribution to the total relaxation, only the first (Ce) and the second (O) nearest neighbors were considered for atomic strain calculations. The atomic strain ε_i for each neighbor ion i associated with vacancy induced relaxation is defined as: $\varepsilon_i = (d^i_{i-v} - d^f_{i-v}) / d^i_{i-v}$, where d^f_{i-v} and d^i_{i-v} is interatomic distance between neighboring ion and vacancy after and before vacancy creation, respectively. The total atomic strain ε_t for vacancy creation is expressed by a summation over all neighboring ions' atomic strain: $\varepsilon_t = \sum_i \varepsilon_i$. The interaction strength parameter, S, can be defined to correlate the atomic strain and relaxation energy via $E_{relax} = \sum_i S_i * \varepsilon_i$. Since Ce-O has different interaction strength than O-O, we can classify S_i into two categories: S_{CO} for Ce-O and S_{OO} for O-O. By comparing the relaxation energies between GB and bulk, we obtain:

$$E_r = E_{seg;relax} = E^{GB}_{relax} - E^{Bulk}_{relax} = S_{CO}\{\sum_i^{Ce(GB)} \varepsilon_i - \sum_i^{Ce(Bulk)} \varepsilon_i\} + S_{OO}\{\sum_i^{O(GB)} \varepsilon_i - \sum_i^{O(Bulk)} \varepsilon_i\} + E_c \quad (4)$$

where $E_{seg;relax}$ or E_r is relaxation contributed segregation energy; E^{GB}_{relax} and E^{Bulk}_{relax} are relaxation energy for GB and bulk, respectively; $\sum_i^{Ce(GB)} \varepsilon_i$ and $\sum_i^{Ce(Bulk)} \varepsilon_i$ are summations over the first nearest neighbor Ce atom's atomic strain at the GB and in bulk, respectively; $\sum_i^{O(GB)} \varepsilon_i$ and $\sum_i^{O(Bulk)} \varepsilon_i$ are summations over the first nearest neighbor O atom's atomic

strain at the GB and in bulk, respectively; and E_c is an energy correction term accounting for the relaxation effect beyond the first and second nearest neighbors. Applying a two-variable linear regression of $E_{seg;relax}$ with respect to $D(Ce) = \sum_i^{Ce(GB)} \varepsilon_i - \sum_i^{Ce(Bulk)} \varepsilon_i$ and $D(O) = \sum_i^{O(GB)} \varepsilon_i - \sum_i^{O(Bulk)} \varepsilon_i$, a very good fitting is achieved with a standard error lower than 3% as shown in Figure 6(b), and the optimal parameter values of S_{CO}=3.88 eV, S_{OO}=-2.40 eV and E_c=-0.42 eV are obtained. Our atomic strain model is capable of rationalizing the relationship between relaxation energy and atomic strain, and hence gives a reliable prediction of the relaxation contributed segregation energies (Figure 6(a)).

In order to identify structural origins for unusually large relaxation in oxygen layers 1 and 2, we determined the layer dependent atomic strain difference D(Ce) and D(O) between the GB and bulk for the nearest neighbor Ce and O ions, as shown in Figure 7(a). At the near-GB region, D(Ce) has a fast drop and becomes negative in oxygen layers 1 and 2. At the far-GB region, positive D(Ce) values are obtained. The negative D(Ce) values were interpreted via displacement vector visualization map in Figure 7(b). Due to the large free-volume space in the GB compared to that in the bulk, Ce ions tend to be attracted towards the GB to further minimize the total free energy after vacancy creation, and results in large inwards-GB displacement vectors, as shown in Figure 7(b). This GB induced relaxation directly leads to the crossover from positive to negative D(Ce) values, and consequently large relaxation energies after vacancy creation, according to our atomic strain model. For far-GB layers, oxygen layers closer to the GB block such GB induced relaxation of Ce ions, and a bulk like behavior is resumed as indicated by Figure 6(a) and Figure 7(a).

3.2 Migration of Oxygen Vacancies in ∑3 GB

Macroscopic oxygen transport involves two critical atomic level processes: oxygen vacancy formation and migration. Activated by thermal agitation and driven by lowering of the total free energy, vacancy formation provides prerequisites for vacancy-assisted migration and allows for thermodynamic prediction of vacancy concentration. On the other hand, vacancy migration is indispensable for shedding light on the kinetic aspects of oxygen transport. In this study, we investigated systematically the migration energy barriers along the lowest migration pathway [100][28] for $V_O^{\cdot\cdot}$. Migration energy barriers for $V_O^{\cdot\cdot}$ near the GB are listed in Table 1, and plotted, along with segregation energies in Figure 8. For layers 0, 1 and 2, it's easier for vacancy to migrate towards (with the E_m of 0.46 to 0.70 eV) than away from (with the E_m of 0.60 to 0.98 eV) the GB. Therefore, if one vacancy forms far away from the GB, it can preferentially hop towards the GB under thermal activation. After equilibration, accumulation of oxygen vacancies at GB is expected, consistent with thermodynamic prediction based on segregation energies (Figure 2). Meanwhile, V_O may be trapped kinetically in near-GB layers due to a high migration barrier of E23=0.98 eV from layer 2 to layer 3. Combining the trend of segregation of V_Os at the GB with lower migration energy barriers (e.g., E01=0.6 eV and E10=0.57 eV) than that in bulk (i.e., 0.75 eV), we can reasonably expect the enrichment of oxygen vacancies near the GB, which may not only facilitate oxygen diffusion in this region owing to increased concentration and decreased migration barrier[30], but also provide potential absorption sites for fission products, such as helium and xenon.

4. Conclusions

Oxygen vacancy's formation and migration in $\Sigma 3\ [1\bar{1}0]/(111)$ grain boundary ceria were systematically investigated based on first principle calculations. Segregation of oxygen vacancies near the GB is favored both thermodynamically and kinetically. The $V_O^{\cdot\cdot}$ defect dominates at low Fermi level and/or oxygen poor conditions, while the $V_O^{\times}$ defect appears at high Fermi level and in oxygen poor conditions. An atomic strain model was proposed to reveal layer dependency of relaxation energies of $V_O^{\cdot\cdot}$. The results indicate that free-volume space induced Ce ion relaxation towards the GB is responsible for the large relaxation energies in oxygen layers 1 and 2. The $V_O^{\cdot\cdot}$ defect preferentially migrates towards the GB and gets trapped at oxygen layers 0, 1 and 2, which in return helps stabilize the GB under low Fermi levels and/or oxygen poor conditions.

These results provide valuable insights into how defects interact with GB, and are useful for engineering GB structures for better ionic, magnetic and chemical properties of nanocrystalline ceria. With decreasing grain size, the contribution of GBs to total oxygen conduction becomes increasingly important. Understanding of defect formation and migration near GB allows prediction of defect concentration and temperature- or pressure-dependent oxygen diffusivities[60], which are essential for assessing GB's influence and developing better SOFC. Furthermore, the knowledge of the relative stability and concentration of oxygen vacancies with different charge and spin-polarized states can facilitate interpretation of ferromagnetism prevalent in NSC[14–16,63]. Last but not

least, the segregation of oxygen vacancies nearby GB impacts oxygen storage capability of NSC and provides sites of high oxygen vacancy concentration crucial for chemical catalyst in automotive industry and water-gas shift reaction[56,64].

Acknowledgement:

This research is supported by the DOE Office of Nuclear Energy's Nuclear Energy University Programs. And the simulations were performed at National Energy Research Scientific Computing Center (NERSC).

References:

(1) Bunluesin, T.; Gorte, R. J.; Graham, G. W. Studies of the Water-Gas-Shift Reaction on Ceria-Supported Pt, Pd, and Rh: Implications for Oxygen-Storage Properties. *Appl. Catal. B Environ.* **1998**, *15*, 107–114.

(2) Heck, R. M.; Farrauto, R. J. Automobile Exhaust Catalysts. *Appl. Catal. Gen.* **2001**, *221*, 443–457.

(3) Fu, Q.; Saltsburg, H.; Flytzani-Stephanopoulos, M. Active Nonmetallic Au and Pt Species on Ceria-Based Water-Gas Shift Catalysts. *Science* **2003**, *301*, 935–938.

(4) Kašpar, J.; Fornasiero, P.; Hickey, N. Automotive Catalytic Converters: Current Status and Some Perspectives. *Catal. Today* **2003**, *77*, 419–449.

(5) Farrauto, R.; Hwang, S.; Shore, L.; Ruettinger, W.; Lampert, J.; Giroux, T.; Liu, Y.; Ilinich, O. New Material Needs for Hydrocarbon Fuel Processing: Generating Hydrogen for the PEM Fuel Cell. *Annu. Rev. Mater. Res.* **2003**, *33*, 1–27.

(6) Cargnello, M.; Doan-Nguyen, V. V. T.; Gordon, T. R.; Diaz, R. E.; Stach, E. A.; Gorte, R. J.; Fornasiero, P.; Murray, C. B. Control of Metal Nanocrystal Size Reveals Metal-Support Interface Role for Ceria Catalysts. *Science* **2013**, *341*, 771–773.

(7) Steele, B. C. H. Mass Transport in Materials Incorporated in Electrochemical Energy Conversion Systems. *Solid State Ion.* **1984**, *12*, 391–406.

(8) Zhang, F.; Chan, S.-W.; Spanier, J. E.; Apak, E.; Jin, Q.; Robinson, R. D.; Herman, I. P. Cerium Oxide Nanoparticles: Size-Selective Formation and Structure Analysis. *Appl. Phys. Lett.* **2002**, *80*, 127–129.

(9) Göbel, M. C.; Gregori, G.; Maier, J. Size Effects on the Electrical Conductivity of Ceria: Achieving Low Space Charge Potentials in Nanocrystalline Thin Films. *J. Phys. Chem. C* **2013**, *117*, 22560–22568.

(10) Patsalas, P.; Logothetidis, S.; Metaxa, C. Optical Performance of Nanocrystalline Transparent Ceria Films. *Appl. Phys. Lett.* **2002**, *81*, 466–468.

(11) Chawla, A. K.; Kaur, D.; Chandra, R. Structural and Optical Characterization of ZnO Nanocrystalline Films Deposited by Sputtering. *Opt. Mater.* **2007**, *29*, 995–998.

(12) Chen, X.; Liu, L.; Yu, P. Y.; Mao, S. S. Increasing Solar Absorption for Photocatalysis with Black Hydrogenated Titanium Dioxide Nanocrystals. *Science* **2011**, *331*, 746–750.

(13) Ramana, C. V.; Mudavakkat, V. H.; Bharathi, K. K.; Atuchin, V. V.; Pokrovsky, L. D.; Kruchinin, V. N. Enhanced Optical Constants of Nanocrystalline Yttrium Oxide Thin Films. *Appl. Phys. Lett.* **2011**, *98*, 031905.

(14) Liu, Y.; Lockman, Z.; Aziz, A.; MacManus-Driscoll, J. Size Dependent Ferromagnetism in Cerium Oxide (CeO_2) Nanostructures Independent of Oxygen Vacancies. *J. Phys. Condens. Matter* **2008**, *20*, 165201.

(15) Fernandes, V.; Mossanek, R. J. O.; Schio, P.; Klein, J. J.; de Oliveira, A. J. A.; Ortiz, W. A.; Mattoso, N.; Varalda, J.; Schreiner, W. H.; Abbate, M.; et al. Dilute-Defect Magnetism: Origin of Magnetism in Nanocrystalline CeO_2. *Phys. Rev. B* **2009**, *80*, 035202.

(16) Chen, S.-Y.; Lu, Y.-H.; Huang, T.-W.; Yan, D.-C.; Dong, C.-L. Oxygen Vacancy Dependent Magnetism of CeO_2 Nanoparticles Prepared by Thermal Decomposition Method. *J. Phys. Chem. C* **2010**, *114*, 19576–19581.

(17) Chen, S.-Y.; Tsai, C.-H.; Huang, M.-Z.; Yan, D.-C.; Huang, T.-W.; Gloter, A.; Chen, C.-L.; Lin, H.-J.; Chen, C.-T.; Dong, C.-L. Concentration Dependence of Oxygen Vacancy on the Magnetism of CeO_2 Nanoparticles. *J. Phys. Chem. C* **2012**, *116*, 8707–8713.

(18) Edmondson, P. D.; Zhang, Y.; Moll, S.; Varga, T.; Namavar, F.; Weber, W. J. Anomalous Grain Growth in the Surface Region of a Nanocrystalline CeO_2 Film under Low-Temperature Heavy Ion Irradiation. *Phys. Rev. B* **2012**, *85*, 214113.

(19) Edmondson, P. D.; Zhang, Y.; Moll, S.; Namavar, F.; Weber, W. J. Irradiation Effects on Microstructure Change in Nanocrystalline Ceria – Phase, Lattice Stress, Grain Size and Boundaries. *Acta Mater.* **2012**, *60*, 5408–5416.

(20) Zhang, Y.; Aidhy, D. S.; Varga, T.; Moll, S.; Edmondson, P. D.; Namavar, F.; Jin, K.; Ostrouchov, C. N.; Weber, W. J. The Effect of Electronic Energy Loss on Irradiation-Induced Grain Growth in Nanocrystalline Oxides. *Phys. Chem. Chem. Phys.* **2014**, *16*, 8051.

(21) Beie, H.; Gnorich, A. Oxygen Gas Sensors Based on CeO_2 Thick and Thin-Films. *Sens. Actuators B-Chem.* **1991**, *4*, 393–399.

(22) Fergus, J. W. Doping and Defect Association in Oxides for Use in Oxygen Sensors. *J. Mater. Sci.* **2003**, *38*, 4259–4270.

(23) Jasinski, P.; Suzuki, T.; Anderson, H. U. Nanocrystalline Undoped Ceria Oxygen Sensor. *Sens. Actuators B-Chem.* **2003**, *95*, 73–77.

(24) Badwal, S. P. S.; Foger, K. Solid Oxide Electrolyte Fuel Cell Review. *Ceram. Int.* **1996**, *22*, 257–265.

(25) Stambouli, A. B.; Traversa, E. Solid Oxide Fuel Cells (SOFCs): A Review of an Environmentally Clean and Efficient Source of Energy. *Renew. Sustain. Energy Rev.* **2002**, *6*, 433–455.

(26) Zhu, W. Z.; Deevi, S. C. A Review on the Status of Anode Materials for Solid Oxide Fuel Cells. *Mater. Sci. Eng. A* **2003**, *362*, 228–239.

(27) Zhou, G.; Shah, P. R.; Montini, T.; Fornasiero, P.; Gorte, R. J. Oxidation Enthalpies for Reduction of Ceria Surfaces. *Surf. Sci.* **2007**, *601*, 2512–2519.

(28) Xiao, H. Y.; Weber, W. J. Oxygen Vacancy Formation and Migration in $Ce_xTh_{1-x}O_2$ Solid Solution. *J. Phys. Chem. B* **2011**, *115*, 6524–6533.

(29) Xiao, H. Y.; Zhang, Y.; Weber, W. J. Stability and Migration of Charged Oxygen Interstitials in ThO_2 and CeO_2. *Acta Mater.* **2013**, *61*, 7639–7645.

(30) Yuan, F.; Zhang, Y.; Weber, W. J. Vacancy–Vacancy Interaction Induced Oxygen Diffusivity Enhancement in Undoped Nonstoichiometric Ceria. *J. Phys. Chem. C* **2015**, *119*, 13153–13159.

(31) Dholabhai, P. P.; Aguiar, J. A.; Wu, L.; Holesinger, T. G.; Aoki, T.; Castro, R. H. R.; Uberuaga, B. P. Structure and Segregation of Dopant–defect Complexes at Grain Boundaries in Nanocrystalline Doped Ceria. *Phys. Chem. Chem. Phys.* **2015**, *17*, 15375–15385.

(32) Murgida, G. E.; Ganduglia-Pirovano, M. V. Evidence for Subsurface Ordering of Oxygen Vacancies on the Reduced CeO_2 (111) Surface Using Density-Functional and Statistical Calculations. *Phys. Rev. Lett.* **2013**, *110*, 246101.

(33) Hojo, H.; Mizoguchi, T.; Ohta, H.; Findlay, S. D.; Shibata, N.; Yamamoto, T.; Ikuhara, Y. Atomic Structure of a CeO_2 Grain Boundary: The Role of Oxygen Vacancies. *Nano Lett.* **2010**, *10*, 4668–4672.

(34) Feng, B.; Hojo, H.; Mizoguchi, T.; Ohta, H.; Findlay, S. D.; Sato, Y.; Shibata, N.; Yamamoto, T.; Ikuhara, Y. Atomic Structure of a Σ3 [110]/(111) Grain Boundary in CeO_2. *Appl. Phys. Lett.* **2012**, *100*, 073109.

(35) Coene, W.; Janssen, G.; Op de Beeck, M.; Van Dyck, D. Phase Retrieval through Focus Variation for Ultra-Resolution in Field-Emission Transmission Electron Microscopy. *Phys. Rev. Lett.* **1992**, *69*, 3743–3746.

(36) Lin, Y.; Wu, Z.; Wen, J.; Poeppelmeier, K. R.; Marks, L. D. Imaging the Atomic Surface Structures of CeO_2 Nanoparticles. *Nano Lett.* **2014**, *14* (1), 191–196.

(37) Esch, F.; Fabris, S.; Zhou, L.; Montini, T.; Africh, C.; Fornasiero, P.; Comelli, G.; Rosei, R. Electron Localization Determines Defect Formation on Ceria Substrates. *Science* **2005**, *309*, 752–755.

(38) Yang, Z.; Woo, T. K.; Baudin, M.; Hermansson, K. Atomic and Electronic Structure of Unreduced and Reduced CeO_2 Surfaces: A First-Principles Study. *J. Chem. Phys.* **2004**, *120*, 7741–7749.

(39) Fabris, S.; de Gironcoli, S.; Baroni, S.; Vicario, G.; Balducci, G. Taming Multiple Valency with Density Functionals: A Case Study of Defective Ceria. *Phys. Rev. B* **2005**, *71*, 041102.

(40) Frayret, C.; Villesuzanne, A.; Pouchard, M.; Matar, S. Density Functional Theory Calculations on Microscopic Aspects of Oxygen Diffusion in Ceria-Based Materials. *Int. J. Quantum Chem.* **2005**, *101*, 826–839.

(41) Nolan, M.; Fearon, J. E.; Watson, G. W. Oxygen Vacancy Formation and Migration in Ceria. *Solid State Ion.* **2006**, *177*, 3069–3074.

(42) Andersson, D. A.; Simak, S. I.; Skorodumova, N. V.; Abrikosov, I. A.; Johansson, B. Optimization of Ionic Conductivity in Doped Ceria. *Proc. Natl. Acad. Sci. U. S. A.* **2006**, *103*, 3518–3521.

(43) Castleton, C. W. M.; Kullgren, J.; Hermansson, K. Tuning LDA+U for Electron Localization and Structure at Oxygen Vacancies in Ceria. *J. Chem. Phys.* **2007**, *127*, 244704.

(44) Andersson, D. A.; Simak, S. I.; Johansson, B.; Abrikosov, I. A.; Skorodumova, N. V. Modeling of CeO2, Ce2O3, and CeO2-X in the LDA plus U Formalism. *Phys. Rev. B* **2007**, *75*, 035109.

(45) Dholabhai, P. P.; Adams, J. B.; Crozier, P.; Sharma, R. Oxygen Vacancy Migration in Ceria and Pr-Doped Ceria: A DFT+U Study. *J. Chem. Phys.* **2010**, *132*, 094104.

(46) Chen, H.-T.; Chang, J.-G. Oxygen Vacancy Formation and Migration in $Ce_{1-x}Zr_xO_2$ Catalyst: A DFT+U Calculation. *J. Chem. Phys.* **2010**, *132*, 214702.

(47) Blöchl, P. E. Projector Augmented-Wave Method. *Phys. Rev. B* **1994**, *50*, 17953–17979.

(48) Kresse, G.; Joubert, D. From Ultrasoft Pseudopotentials to the Projector Augmented-Wave Method. *Phys. Rev. B* **1999**, *59*, 1758–1775.

(49) Kresse, G.; Hafner, J. \textit{Ab Initio} Molecular Dynamics for Liquid Metals. *Phys. Rev. B* **1993**, *47*, 558–561.

(50) Kresse, G.; Hafner, J. Ab Initio Molecular-Dynamics Simulation of the Liquid-Metal–amorphous-Semiconductor Transition in Germanium. *Phys. Rev. B* **1994**, *49*, 14251–14269.

(51) Kresse, G.; Furthmüller, J. Efficiency of Ab-Initio Total Energy Calculations for Metals and Semiconductors Using a Plane-Wave Basis Set. *Comput. Mater. Sci.* **1996**, *6*, 15–50.

(52) Kresse, G.; Furthmüller, J. Efficient Iterative Schemes for Ab Initio Total-Energy Calculations Using a Plane-Wave Basis Set. *Phys. Rev. B* **1996**, *54*, 11169–11186.

(53) Perdew, J. P.; Zunger, A. Self-Interaction Correction to Density-Functional Approximations for Many-Electron Systems. *Phys. Rev. B* **1981**, *23*, 5048–5079.

(54) Dudarev, S. L.; Botton, G. A.; Savrasov, S. Y.; Humphreys, C. J.; Sutton, A. P. Electron-Energy-Loss Spectra and the Structural Stability of Nickel Oxide: An LSDA+U Study. *Phys. Rev. B* **1998**, *57*, 1505–1509.

(55) Monkhorst, H. J.; Pack, J. D. Special Points for Brillouin-Zone Integrations. *Phys. Rev. B* **1976**, *13*, 5188–5192.

(56) Paier, J.; Penschke, C.; Sauer, J. Oxygen Defects and Surface Chemistry of Ceria: Quantum Chemical Studies Compared to Experiment. *Chem. Rev.* **2013**, *113*, 3949–3985.

(57) Momma, K.; Izumi, F. *VESTA* : A Three-Dimensional Visualization System for Electronic and Structural Analysis. *J. Appl. Crystallogr.* **2008**, *41*, 653–658.

(58) Kröger, F. A.; Vink, H. J. Relations between the Concentrations of Imperfections in Crystalline Solids. In *Solid State Physics*; Turnbull, F. S. and D., Ed.; Academic Press, 1956; Vol. 3, pp 307–435.

(59) Henkelman, G.; Uberuaga, B. P.; Jónsson, H. A Climbing Image Nudged Elastic Band Method for Finding Saddle Points and Minimum Energy Paths. *J. Chem. Phys.* **2000**, *113*, 9901–9904.

(60) Zacherle, T.; Schriever, A.; De Souza, R. A.; Martin, M. \textit{Ab Initio} Analysis of the Defect Structure of Ceria. *Phys. Rev. B* **2013**, *87*, 134104.

(61) Tuller, H. L.; Nowick, A. S. Small Polaron Electron Transport in Reduced CeO_2 Single Crystals. *J. Phys. Chem. Solids* **1977**, *38*, 859–867.

(62) Liu, B.; Cooper, V. R.; Zhang, Y.; Weber, W. J. Segregation and Trapping of Oxygen Vacancies near the SrTiO3 Σ3 (112) Tilt Grain Boundary. *Acta Mater.* **2015**, *90*, 394–399.

(63) Ge, M. Y.; Wang, H.; Liu, E. Z.; Liu, J. F.; Jiang, J. Z.; Li, Y. K.; Xu, Z. A.; Li, H. Y. On the Origin of Ferromagnetism in CeO_2 Nanocubes. *Appl. Phys. Lett.* **2008**, *93*, 062505.

(64) Gorte, R. J. Ceria in Catalysis: From Automotive Applications to the Water–gas Shift Reaction. *AIChE J.* **2010**, *56*, 1126–1135.

Tables:

Table 1 Migration energy barriers for +2 charged V_O near the ∑3 grain boundary in ceria.

Path	E_m (eV)	Path	E_m (eV)
E01	0.60	*E10*	0.57
E12	0.70	*E21*	0.46
E23	0.98	*E32*	0.70
E34	0.70	*E43*	0.82
E45	0.76	*E54*	0.84

Figures:

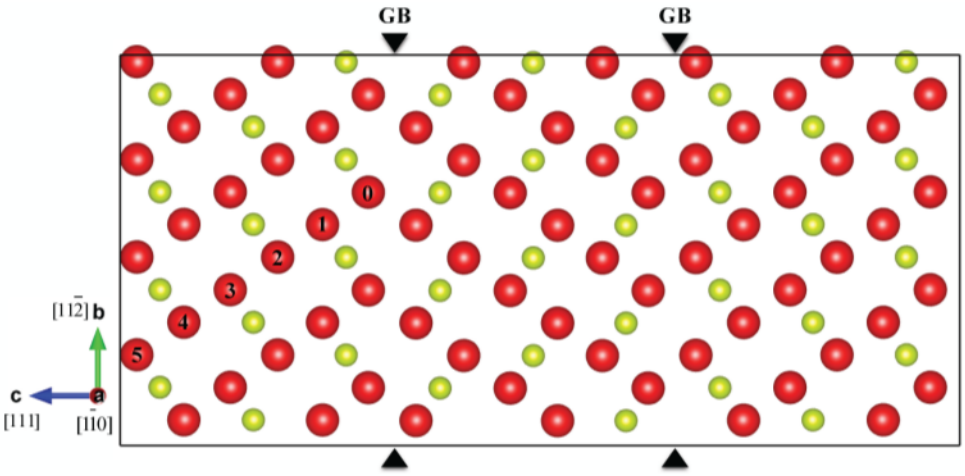

Figure 1. Projected view along $[1\bar{1}0]$ axis of ∑3 grain boundaries. O layers are labeled by integers from 0 to 5. Layer 0 lies on one of two grain boundaries indicated by black triangles.

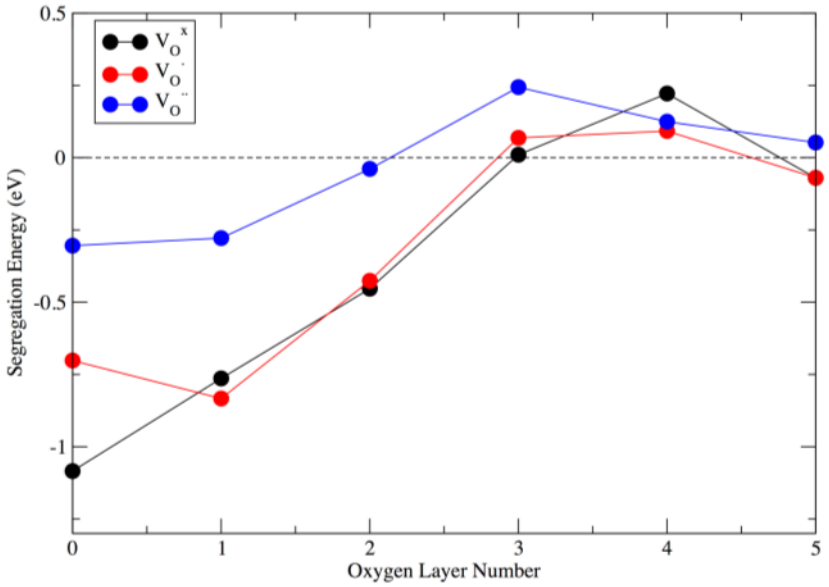

Figure 2. Segregation energy for +2, +1 and 0 charged oxygen vacancies versus oxygen layer number. The black dashed line indicates the bulk limit.

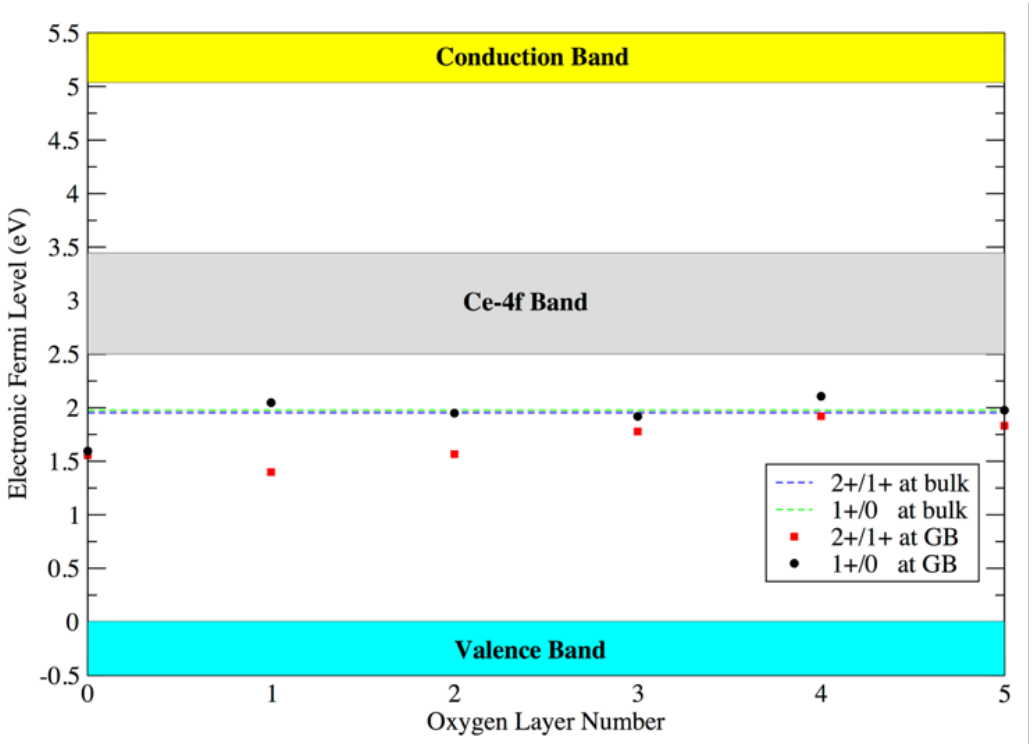

Figure 3. Thermodynamic transition levels for oxygen vacancy as a function of oxygen layer number in bulk and at the ∑3 grain boundary in ceria.

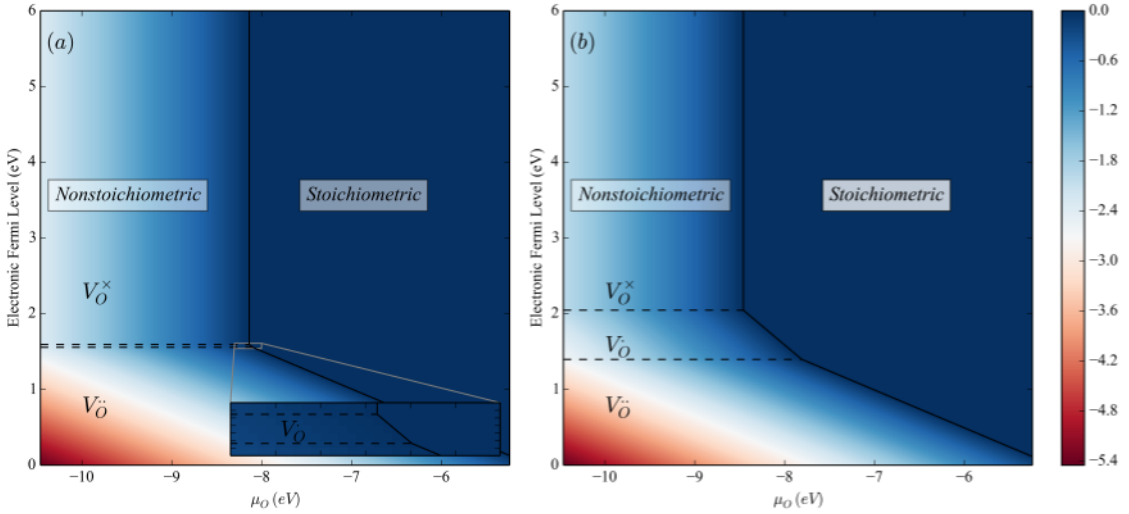

Figure 4. Chemical potential and Fermi energy dependent oxygen vacancy formation energies near the ∑3 grain boundary ceria at (a) the GB layer (layer 0) and (b) the first nearest neighbor layer (layer 1). The legend is in unit of eV.

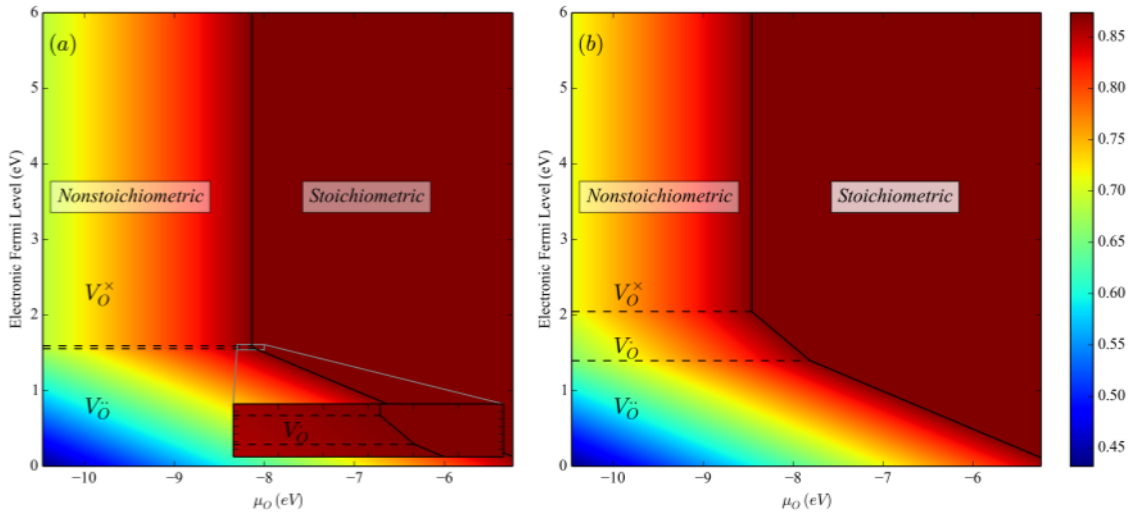

Figure 5. Chemical potential and Fermi energy dependent grain boundary formation energies near the ∑3 grain boundary ceria with a single oxygen vacancy at (a) the GB layer (layer 0) and (b) the first nearest neighbor layer (layer 1). The legend is in unit of J/m^2.

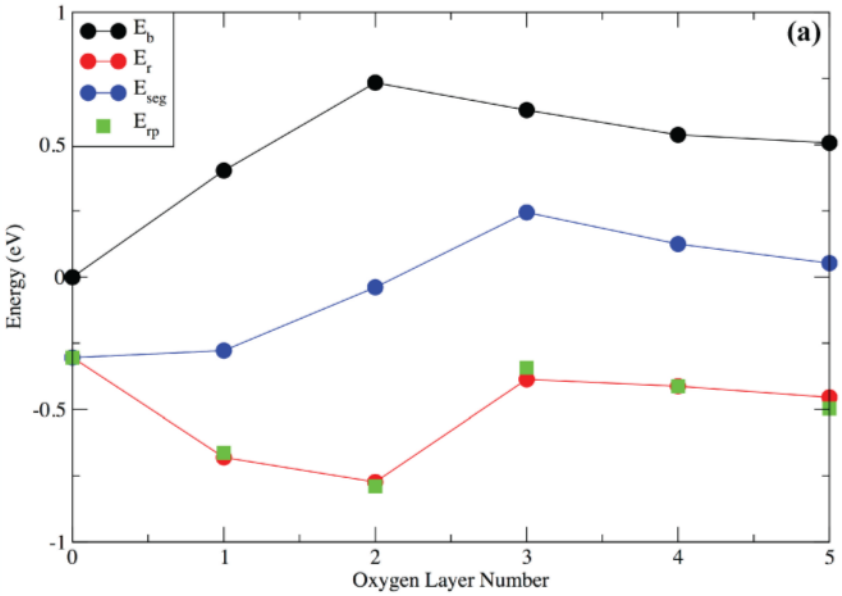

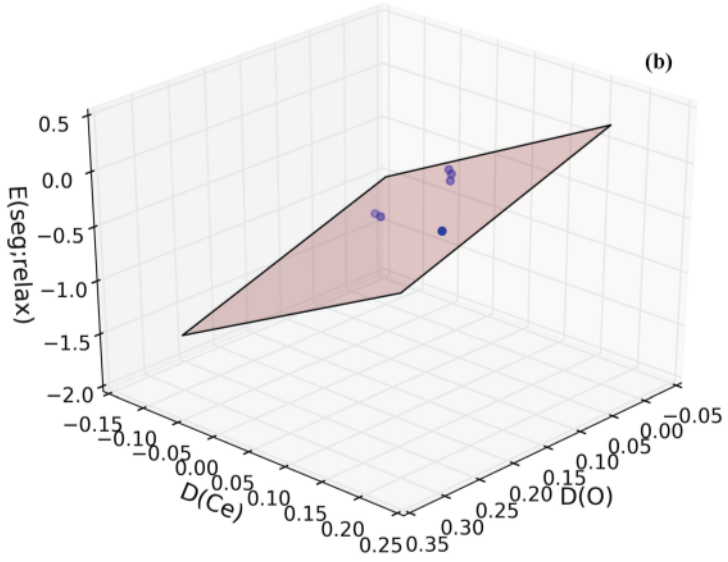

Figure 6. (a) Oxygen layer dependent total (solid black circles), relaxation contributed (solid red circles) and bonding contributed (solid blue circles) segregation energies of oxygen vacancy. Atomic strain model predicted relaxation contributed segregation energies, E_{rp},

are included for comparison (solid green squares). (b) Two-variable linear regression plot in atomic strain model, where blue dots are relaxation contributed segregation energies and the plane enclosed by black edges is a fitting result according to Eq. 4.

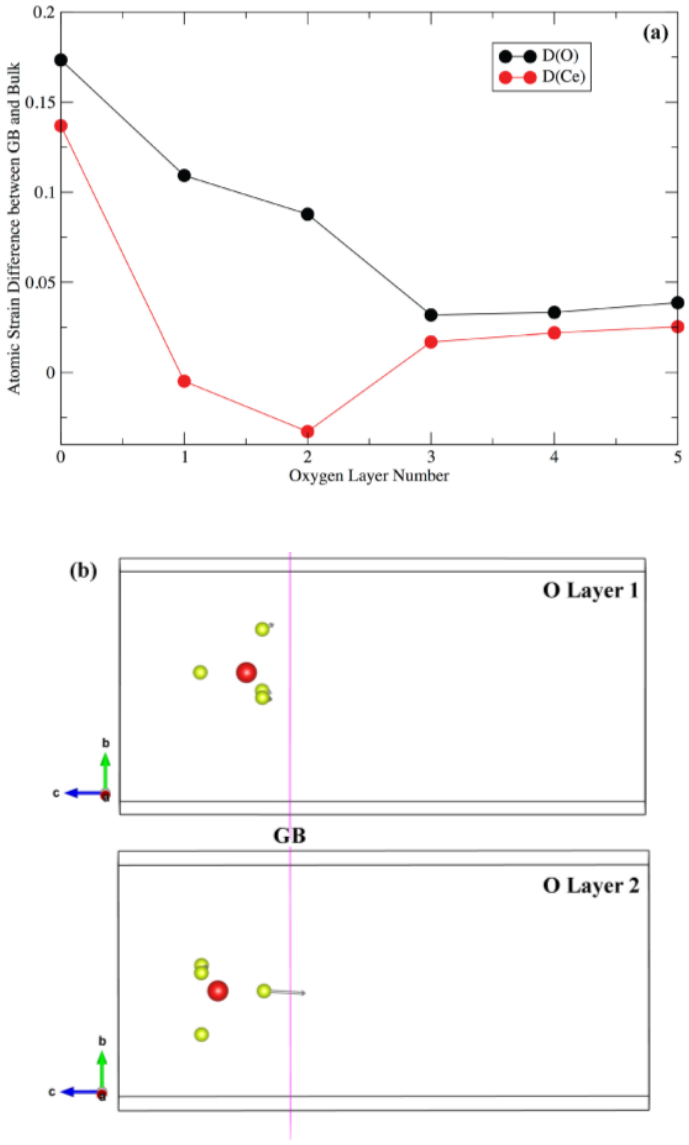

Figure 7. (a) Oxygen layer dependent atomic strain difference D(Ce) and D(O). (b) Displacement vector visualizations of the nearest neighbor Ce ions (yellow balls) surrounding O vacancy (red balls) at O layers 1 and 2. The location of the grain boundary

is indicated by pink line. The atomic displacement vectors shown by grey colors are magnified by 10 times for better visualization.

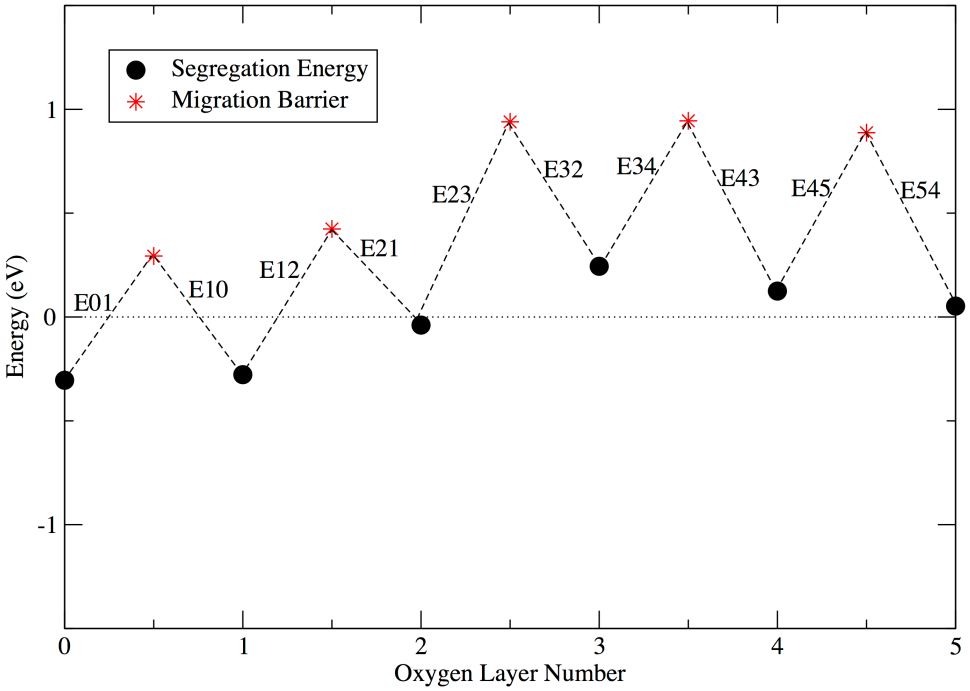

Figure 8. Migration energy barrier (red stars) and segregation energies (solid black circles) for +2 charged oxygen vacancy as a function of oxygen layer from the ∑3 grain boundary in ceria. The zero energy line represents the bulk limit, where segregation energy is zero. Eij gives the migration energy barrier of vacancy migration from layer i to layer j.

Graphic Abstract

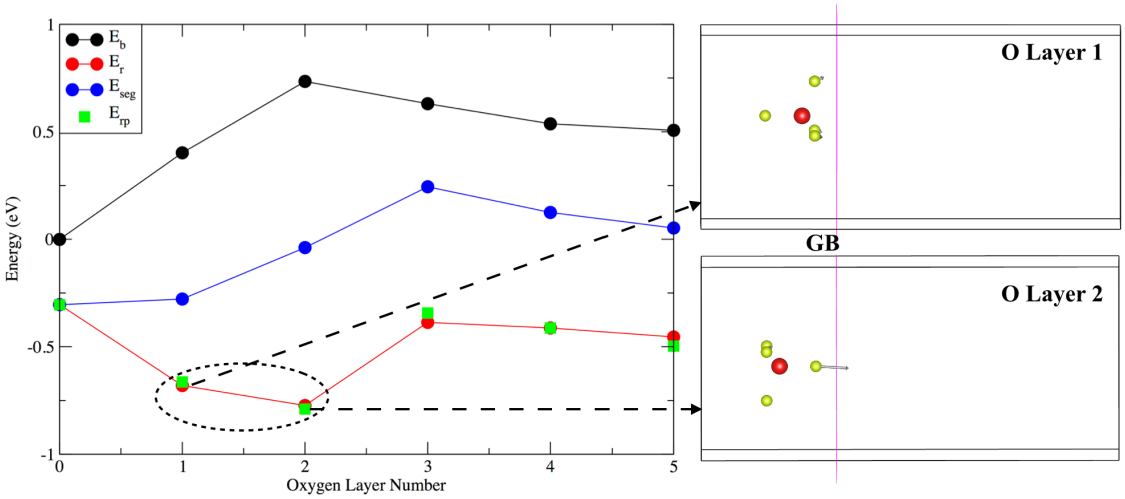

The segregation energies of +2 charged oxygen vacancies transition from negative values at oxygen layers 0,1,2 to positive values beyond layer 2. The GB-induced large relaxation of Ce ions accounts for large negative values of ion relaxation energies, resulting in a preferential segregation of oxygen vacancies nearby grain boundary.